ID18F: A new micro–X-ray fluorescence end-station at the European Synchrotron Radiation Facility (ESRF): Preliminary results

ARTICLE *in* X-RAY SPECTROMETRY · JULY 2001

Impact Factor: 1.35 · DOI: 10.1002/xrs.494

X-RAY SPECTROMETRY
X-Ray Spectrom. 2001; **30**: 242–252

ID18F: a new micro-x-ray fluorescence end-station at the European Synchrotron Radiation Facility (ESRF): preliminary results

A. Somogyi,[1*,†] M. Drakopoulos,[2] L. Vincze,[1] B. Vekemans,[1] C. Camerani,[3] K. Janssens,[1] A. Snigirev[2] and F. Adams[1]

[1] Micro- and Trace Analysis Centre, University of Antwerp, Universiteitsplein 1, B-2610 Wilrijk-Antwerp, Belgium
[2] ID22 ESRF, BP 220, F-38043 Grenoble Cedex, France
[3] Department of Environmental and Inorganic Chemistry, Chalmers University of Technology, S-41296 Göteborg, Sweden

Received 1 December 2000; Accepted 9 March 2001

A new user end-station is under construction at the ESRF with collaboration between the Micro-Fluorescence, Imaging and Diffraction beamline (ID22) and the Micro and Trace Analysis Center (MITAC) of the University of Antwerp. The new end-station is dedicated to quantitative micro-fluorescence measurements. The analytical characteristics (degree of polarization of the incoming beam, absolute and relative detection limits) of the new set-up were investigated during preliminary experiments by using a temporary experimental set-up. Copyright © 2001 John Wiley & Sons, Ltd.

INTRODUCTION

During the last decade, a number of practical and sensitive microscopic analytical methods [e.g. secondary ion microscopy and imaging (SIMS), x-ray photoelectron spectroscopy (XPS), micro-Auger microscopy, micro-proton-induced x-ray emission (μ-PIXE) and micro-x-ray fluorescence analysis (μ-XRF)] have been developed. For many applications these microanalytical methods of analysis are relative methods, i.e. the signal measured requires reference measurements on a certified or standard reference material (CRM or SRM) or a comparison with a quantitatively more reliable, if possible absolute, method of analysis. However, these instrumental developments were not followed by an increase in the availability of CRMs for trace element analysis at the microscopic level. Although several CRMs and SRMs have been developed and are available for macroscopic 'bulk' measurements, only a few have been produced for microscopic analysis so far.

For the elaboration of CRMs in the future, at least one absolute (primary) method of analysis is necessary to link the results of chemical measurements to the SI system of units. Within the range of microbeam methods of analysis, μ-XRF is probably the analytical method of choice for being developed as a certification or calibration tool and as a reference tool for other microanalytical techniques. The major reason for this is that the interaction of x-rays with matter is completely understood and supported by high-quality physical data. A realistic goal is to reach an average accuracy of quantification in the range 3–5% for micrometer-sized objects or portions of larger objects at sub-ppm quantification limits. This accuracy corresponds to the present limit of accuracy of the physical constants governing the x-ray interaction process. These characteristics can only be achieved with focused synchrotron radiation (SR)-based sources of x-rays of the so-called third generation.

In order to improve the capabilities of μ-SRXRF as a method for quantitative and non-destructive elemental analysis of micro-heterogeneous materials, a highly stable end-station (ID18F) is under construction at the ESRF with collaboration between the Micro-Fluorescence, Imaging and Diffraction beamline (ID22) and the Micro and Trace Analysis Center (MITAC) of the University of Antwerp. The new end-station is dedicated to quantitative experiments and will be situated in the third μ-XRF experimental hutch of the ID18 nuclear resonance beamline and share its optics infrastructure. The goal of the new end-station is to develop and to improve the procedures of μ-XRF to reach an average accuracy of quantification in the range 3–5% for elements above atomic number 13 down to concentration levels below 1 ppm. In order to achieve this goal, the user end-station requires a high reproducibility of the set-up (both the measurement geometry and the instrumental parameters) and very good short- and long-term stability. In order to characterize the analytical characteristics of the new μ-XRF end-station (degree of polarization, absolute and relative limits of detection), SRMs and CRMs were measured under different experimental conditions.

THE ID18F USER END-STATION

The new end-station is working in the third experimental hutch of the ID18 nuclear resonance beamline[1] of the European Synchrotron Radiation Facility (ESRF, Grenoble,

*Correspondence to: A. Somogyi, ID22 ESRF, BP 220, F-38043 Grenoble Cedex, France. E-mail: Somogyia@esrf.fr
†On leave from Isotope Laboratory, Kossuth University, H-4010 Debrecen, Hungary.

DOI: 10.1002/xrs.494

France). In Fig. 1 a schematic layout of the ID18 beamline and the ID18F user end-station is shown. The end-station uses the three undulators of the ID18 beamline (see Table 1), which provides tuning of the excitation radiation in the 6–27 keV energy range: one undulator provides an x-ray beam of 14.4 keV in the fundamental and two identical undulators can be tuned between 6 and 9 keV in the fundamental and between 21.5 and 27 keV in the third harmonic. The two identical undulators may be used separately to obtain a smaller microbeam at the sample position, or when used together achieve approximately double flux in the focused beam at a somewhat larger beam size. A fixed exit double crystal Si(111) monochromator is used for defining the energy of the monochromatic excitation radiation with an energy resolution of $\Delta E/E = 10^{-4}$. In order to reduce the absorption of the x-ray beam in the air path between the optics hutch and the third experimental hutch, vacuum tubes can be installed.

A schematic layout of the microprobe set-up, which is positioned on a movable granite table in the experimental hutch, is shown in Fig. 2. For the demagnification of the synchrotron source and to create the microbeam, a Fresnel zone plate[2,3] (FZP) or a compound refractive lens (CRL)[4,5] can be employed, depending on the energy and beam size requirements of the experiment. The advantages of using FZP and CRL as focusing devices compared with other techniques (such as capillaries, Kirpatrick–Baez mirrors, etc.) are that they are in-line focusing elements, they do not destroy the coherence of the synchrotron beam, the lens–sample distance is large (in the range 0.5–1.5 m) and they are easy to align. The size of the demagnified source depends on the type of

Table 1. Beamline characteristics of the ID18 beamline

Parameter	Undulator 1 optimum, 14.4 keV	Undulators 2 and 3 optimum, 21.5 keV
Magnet period (mm)	22.8	34
Energy range (keV)	14.4	6–9, 21.5–27
Number of periods	72	48
K (at 20 mm gap)	0.256	0.857
Field B_{max} (T)	0.12	0.16
Source size ($H \times V$) FWHM (μm)	812 × 54	812 × 54
Source divergence ($H \times V$) FWHM (μrad)	28 × 4	28 × 4
Beam size at 30 m ($H \times V$) FWHM (mm)	1.8 × 0.6	1.8 × 0.5

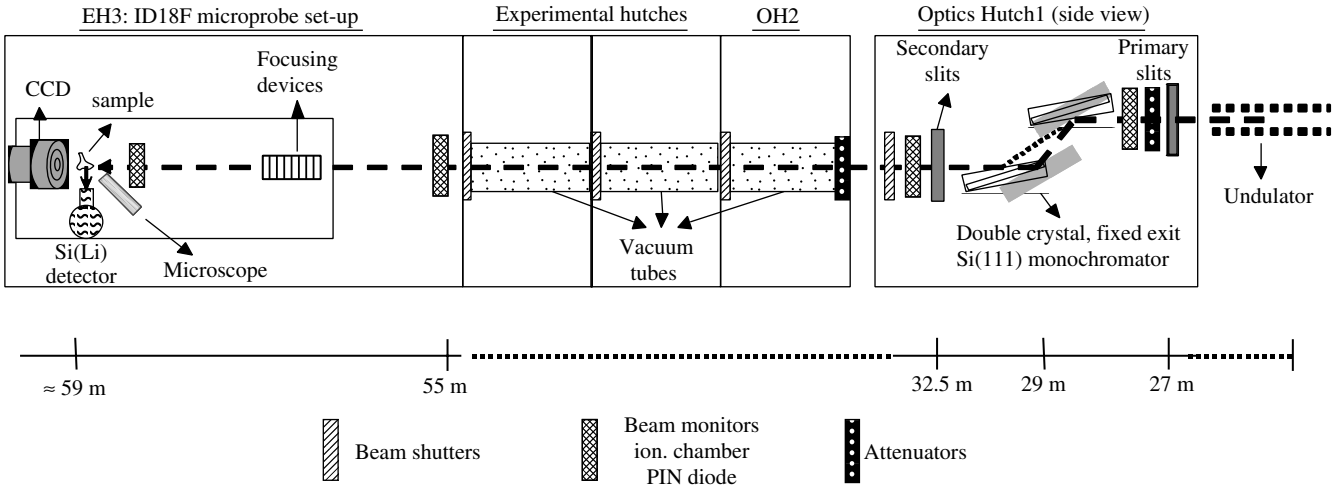

Figure 1. Schematic layout of the ID18 beamline and the ID18F user end-station.

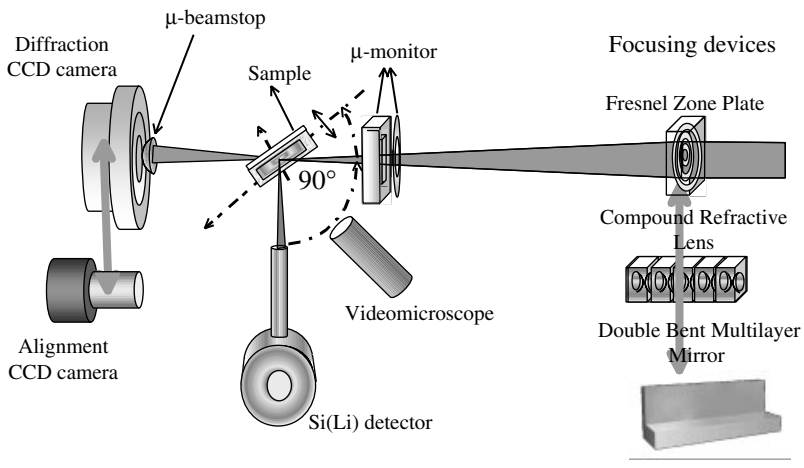

Figure 2. Schematic layout of the microprobe set-up (top view, not to scale).

XRS

focusing device used and typically is in the 1–5 μm region vertically and in the 12–15 μm region horizontally. The FZP is used for focusing at 14.4 keV or at lower energies.

In Fig. 3, the electron microscope image of the FZP used during the preliminary experiments is shown together with the intensity distribution of the focused beam measured at the image plane by a high-resolution CCD camera. The focal distance, f, of the FZP is determined by its geometric characteristics and by the energy of the incoming beam:

$$f = \frac{r_n^2 - r_{n-1}^2}{\lambda} \approx \frac{2r_n d_n}{\lambda} \tag{1}$$

where r_n and d_n are the radius and the width of the nth zone of the FZP, respectively, and λ is the wavelength of the incoming radiation.

The size of the demagnified source s_{mb} can be calculated from the size of the source s_s by using direct analogy with the thin lens equation:

$$s_{mb} = \frac{d_{im,FZP}}{d_{s,FZP}} s_s = \frac{f}{d_{s,FZP} - f} s_s \tag{2}$$

where $d_{im,FZP}$ and $d_{s,FZP}$ are the distances of the image plane and the undulator source from the FZP, respectively.

At higher energies (21.5–27 keV), parabolic compound refractive lenses (CRL)[5] are used as focusing devices. CRLs work similarly to thin optical focusing lenses but since the real part of the refractive index of x-rays in matter $(1 - \delta)$ is <1, the focusing lens should have a concave form. As the refractive index decrement δ is a very small positive value of the order of 10^{-6}, the refraction is very weak. This results in a very small deflection of the x-ray lens, and therefore a large number of lenses must be used for efficient focusing. On the other hand, x-rays are strongly absorbed in matter, resulting in low transmission through matter of thickness in the millimeter range. In order to achieve an appropriate focal length and spot size with an appropriate efficiency, a set of well-aligned thin individual lenses should be used as a focusing lens in the x-ray region. After the first lenses, which had crossed-cylindrical symmetry,[3] new lenses having a parabolic profile and rotational symmetry around the optical axis have been developed which focus in two directions and are free of spherical aberration.

A schematic drawing of the CRL is given in Fig. 4. The focal length f measured from the middle of the lens depends on the geometric parameters of the parabola defining the lenses, the number of individual lenses N forming the compound lens and the energy of the incoming beam (through δ):

$$f = \frac{R}{2N\delta} \tag{3}$$

where R is the radius of the curvature of the apex of the parabola. The term δ is related to the refractive index, n, through

$$n = 1 - \delta - i\beta \tag{4a}$$

$$\delta \approx \frac{N_A r_0 Z}{2\pi A} \rho \lambda^2, \qquad \beta = \frac{\lambda \mu^*}{4\pi} \tag{4b}$$

where N_A is Avogadro's number, r_0 is the classical electron radius, Z, A and ρ are the atomic number, atomic mass and the density of the lens material, respectively, and μ^* is the linear absorption coefficient.

The large focal distances (0.5–2 m) of the above-described in-line focusing devices result in free space around the sample which makes it easy to place other devices such as beam intensity monitors (see Fig. 5) in the focused beam close to the sample. The size of the beam at the sample position can easily be increased by moving the sample out of the image plane.

The sample is mounted on the sample stage containing one rotation and three translation motor stages. With the rotation stage the angle of incidence to the sample surface can be determined. The sample can be scanned in the horizontal and vertical directions and it can be fully aligned into the image or focal plane of the focusing devices by the three translation stages. The horizontal and vertical scanning range

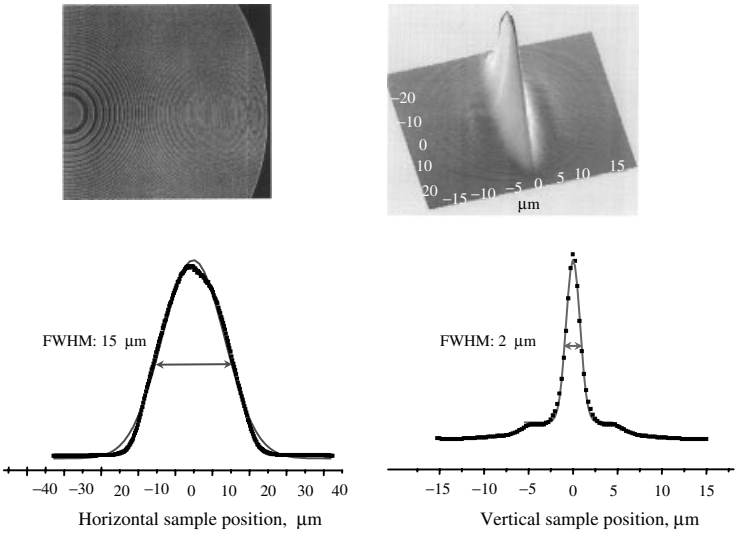

Figure 3. Electron microscopic image of the Fresnel zone plate (FZP) used during the preliminary experiments. Intensity distribution of the focused beam was measured by a CCD camera.

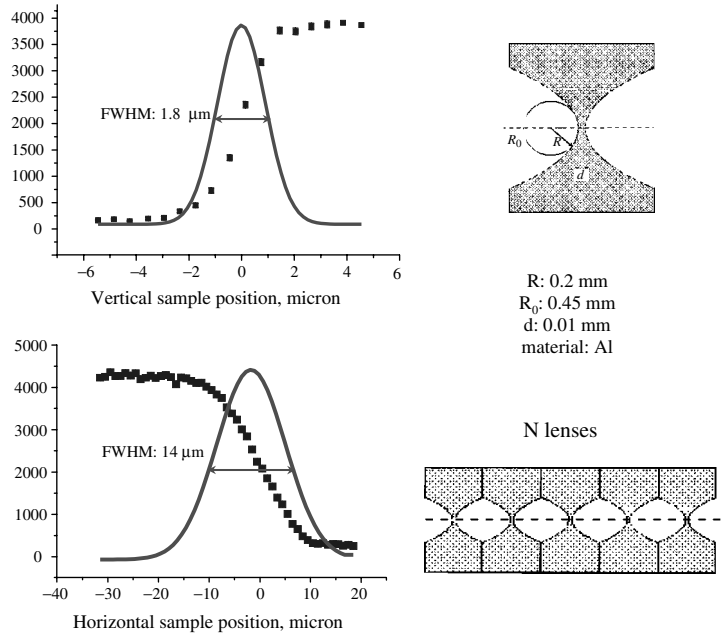

Figure 4. Schematic diagram of the compound refractive lens (CRL) and the result of the knife-edge scan of an Au knife-edge sample with a CRL lens consisting of 63 lenses.

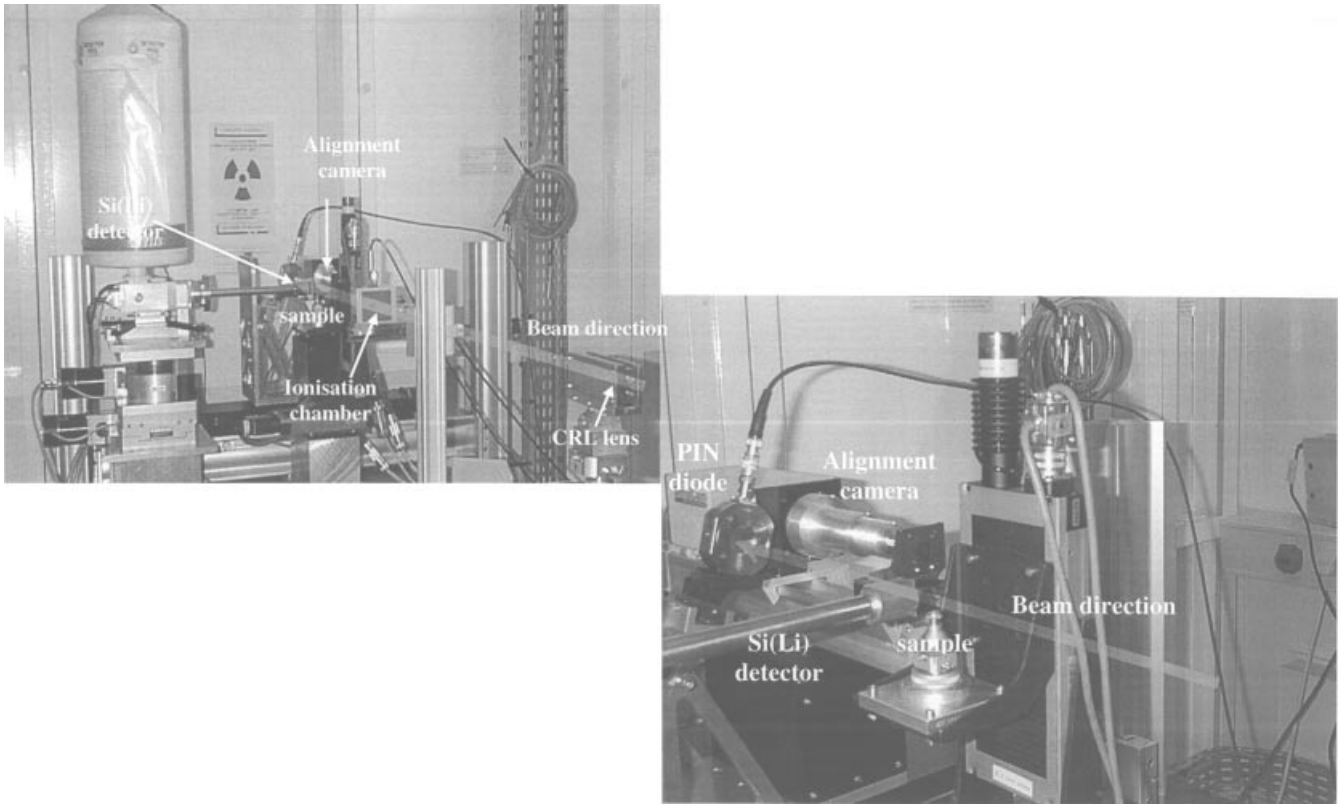

Figure 5. ESRF's ID18F user end-station: preliminary experimental set-up.

is 50 × 50 mm. The step sizes of the horizontal and vertical translation are 1 and 0.1 μm, respectively.

The characteristic x-ray line intensities of the sample are detected by a Si(Li) detector of 30 mm^2 active area, 3.5 mm active thickness and having an 8 μm thick Be window. The semiconductor detector is placed in 90° geometry to the incoming linearly polarized x-ray beam in the storage beam plane in order to minimize the intensity of the scattered peaks in the spectra. The detector itself is placed on motorised translation stages, allowing for micrometer-sized optimization of the detection position. Different detectors such as an ionization chamber and a PIN diode (see Fig. 5) will be used in order to monitor the intensity of the incoming and focused beam. A videomicroscope and a high-resolution CCD camera allow for the easy alignment of the sample and the microprobe set-up. Optionally, the use of a diffraction

camera allows small- and large-angle scattering together with the XRF measurements.

THEORETICAL

One of the most important characteristics of the microprobe set-up is the lower limit of detection (LD). The absolute and relative limits of detection can be determined by measuring CRMs with well-known elemental composition.

$$C_{\mathrm{MDL},i} = \frac{3\sigma_{i,\mathrm{bgr}}}{N_i} C_i = \frac{3\sqrt{I_{i,\mathrm{B}}}}{I_i\sqrt{t}} C_i \qquad (5)$$

where $C_{\mathrm{MDL},i}$ is the detection limit of element i with 99.86% confidence level, in ppm or mg cm^{-2}, $\sigma_{i,\mathrm{bgr}}$ is the standard deviation of the background intensity measured under the characteristic x-ray peak of element i, N_i is the net peak area of element i in counts, $I_{i,\mathrm{B}}$ and I_i are the measured background and characteristic x-ray intensity of element i in counts per second, t is the live time and C_i is the concentration of element i in the standard sample in ppm or mg cm^{-2}.

The LD is determined by the peak-to-background ratio and by the measurement time. The overall background of an x-ray spectrum depends on the degree of polarization of the incoming beam, on the measurement geometry (angle of detection, sample–detector distance, diameter of the detector collimator, air path seen by the detector), on the characteristics of the sample (matrix composition, density and thickness) and on the characteristics of the semiconductor detector (see later).

The scattering intensity depends strongly on the degree of polarization of the impinging radiation. Synchrotron radiation from an undulator source is linearly polarized in the plane of the electron orbit. The polarization of the radiation influences the angular distribution of the scattered photons in such a way that the scatter background in the ED-XRF spectra is minimized when the detector is placed at a 90° angle to the incident beam, in the plane of polarization. The degree of polarization was determined by Monte Carlo simulation. Two spectra of the sample corresponding to 100% vertical and 100% horizontal polarization were simulated and their linear combination was compared with the experimental spectrum. The details of the calculations can be found elsewhere.[6]

The background of the spectra is also affected by the response function of the semiconductor detector. The low-energy peak tailing is highly dependent on the technology of the detector manufacture and on the electrical contacts of the detector. Incomplete charge collection caused by the escape of electrons through the contacts and edges of the detector may cause a significant increase in the detector low-energy tailing and in the continuous background. For the measurements of the characteristic x-ray line intensities in the region below 30 keV energy two different types of liquid nitrogen-cooled semiconductor detectors have been considered: Si(Li) and HPGe. Owing to the lower atomic number of Si the absorption in the dead layer is smaller than for HPGe but the detection efficiency of the Si(Li) detector decreases above 20 keV because the absorption of higher energy x-rays is less effectient. Recently, the significant decrease in the thickness of the dead layers of the state-of-the-art semiconductor detectors and the inherently better energy resolution let to the HPGe detector becoming the instrument of choice even in the energy region below 30 keV. One disturbing effect in the spectra of Ge detectors is the more prominent escape peak. The relative intensity of the escape peak of Si is ~1% at 3 keV parent peak energy and the ratio decreases rapidly with increasing energy. In the case of HPGe the relative intensity of the escape peak is ~16% at 12 keV and remains of the order of 4% at 30 keV.

The peak-to-background ratio is also affected by the measurement geometry. The most important factors influencing the peak-to-background ratio at a fixed detection angle are the solid angle of detection, the sample–detector distance and the air path seen by the detector. The ID18F μ-XRF set-up should be able to measure very different types of samples varying from microscopic samples to parts of macroscopic objects resulting in a large variation of the count rate impinging on the semiconductor detector. Si(Li) and HPGe detectors cannot handle very high count rates in excess of 80 000–100 000 counts s^{-1} because of the very high dead time and distortions of the spectra. Hence, in order to achieve appropriate real-time and non-distorted measured spectra, the count-rate impinging on the detector needs to be optimized by changing the solid angle of detection or by using absorbers. The solid angle of detection can be varied either by using collimators with different entrance hole diameters and/or by changing the sample detector distance. In the case of a collimator with larger hole diameter the intensity of the scattered radiation reaching the detector increases, and by increasing the distance between the sample and the detector the absorption of the characteristic x-ray lines of the light elements will become larger. The geometric size and edge effect of the detector, resulting in a significant increase of the background, also affect the optimum collimator hole diameter.

EXPERIMENTAL

The following experiments were performed using monochromatic radiation at two different energies: 14.4 and 21 keV. An FZP was used as a focusing device at 14.4 keV. This FZP consists of 620 zones and its aperture is 620 μm, the radius of the first zone being $R = 12.45$ μm and the width of the last zone 0.25 μm. The zone material is gold of 1.5 μm thickness on a substrate of Si_3N_4 of 2 μm. A CRL containing 63 individual parabolic Al lenses was used at 21 keV for creating the micro-beam. The aperture of the lens was 450 μm, the apex of the parabola was 200 μm and the thickness of the material at the middle of the lens was 10 μm. A high-resolution CCD camera and Au knife edge sample were used to determine the size of the focused beam.

The intensities of the incoming and the focused beam were monitored using ionization chamber detectors (OKEN, 3 cm length) during the measurements. The intensity of the focused beam was used for normalizing the measured x-ray intensities of the sample. Both Si(Li) and HPGe detectors were used for detecting the characteristic x-ray line intensities. The three detectors applied during the

measurements were (a) an HPGe (PGT) detector of 30 mm^2 active area, 5.5 mm effective thickness, 3000 Å thick polymer window with 400 Å Al layer on a Si grid (380 μm thick and 64 μm wide Si ribs, 250 μm pitches) (MOXTEK window), (b) a Gresham Si(Li) detector of 30 mm^2 active area, 3.5 mm thickness, 8 μm Be window and (c) a Eurysis Si(Li) detector of 12 mm^2 active area, 4.2 mm active thickness, 8 μm Be window. A Tennelec TC245 spectroscopy amplifier, a Canberra 9635 ADC and a Canberra 556A AIM (multi-channel analyser) were used for collecting the spectra. The AXIL software package[7,8] was used for spectrum evaluation.

The SRM 1832 (0.55 μm thin glass) and SRM 1577 (bovine liver) were used for the measurement of the analytical characteristics of the beamline under different experimental conditions. A pellet of 10 mm diameter and 1 mm thickness was pressed from SRM 1577 for the measurements. The angle of incidence between the excitation beam and the surface of the sample was 45°. The average detection angle was 90° to the direction of the incident beam.

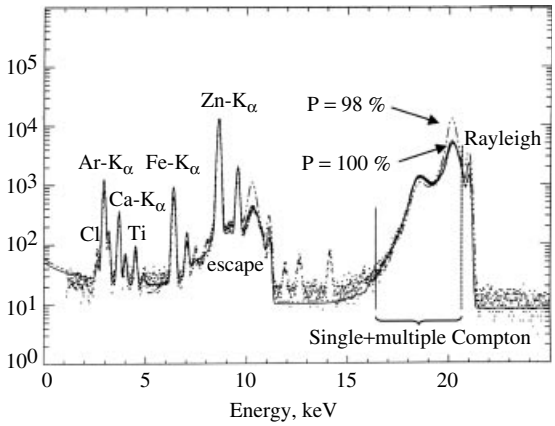

Figure 6. Measured and simulated spectra of a 420 μm thick polypropylene disk (live time 300 s). Estimated degree of linear polarization >99.5%. Dotted line measured spectrum; solid and dot-dashed lines, simulated spectra corresponding to $P = 100$ and 98% degree of polarization, respectively.

RESULTS AND DISCUSSION

In order to calculate the absolute limit of detection it is necessary to know precisely the size of the focused beam at the sample position in order to derive the illuminated sample volume and mass. The focused beam-size produced by the FZP at 14.4 keV energy was determined with a CCD camera positioned in the image plane of the FZP. From the image of the focused beam (Fig. 3), the horizontal and vertical spot sizes, 15 and 2 μm, respectively, were determined. The calculated vertical spot size in the case of 14.4 keV radiation and 56 m source–FZP distance is 1.79 μm [See Eqn (2)]. At 21 keV excitation energy the focused beam was obtained by the CRL. The size of the demagnified source was measured by scanning the Au knife-edge sample in horizontal and vertical directions (see Fig. 4) in the image plane of the CRL. The size of the image of the source was 14 and 1.8 μm in the horizontal and vertical directions, respectively. The theoretical vertical source size calculated from Eqns (2) and (3) is 1.3 μm.

In order to determine the degree of polarization of the incoming beam, a polypropylene disk of 420 μm thickness, with known density and composition, was measured in a given and fixed measurement geometry (45° incident and detection angle to the surface of the sample and an average angle of detection of 90° to the incoming beam). The ratio of the scattered peak intensities to that of the fluorescence lines is dependent on the degree of polarization of the primary x-ray beam. In Fig. 6, the measured and simulated spectra at two different degrees of polarization (98 and 100%) are shown. From the intensities of the scattered peaks, which depend very sensitively on small changes in the degree of polarization, a degree of polarization of 99.5% was deduced.

In order to test which type of semiconductor detector provides the best LDs in the 6–27 keV energy region, different standard reference materials were measured with the Si(Li) detector at 21 keV and with the HPGe detector at 14.4 and 21 keV under similar measurement geometry. The intensity of the incident beam was of the order of 10^9 photons s^{-1} in the focused beam. In Fig. 7(a)–(d) the x-ray spectra of the SRM 1577 and the SRM 1832 standards are shown. The spectra are normalized to the same total counts in order to show the differences in the peak to background ratio. It is clear that the background of the Si(Li) detector at energies below 8 keV is significantly higher than that of the HPGe detector but that the escape peaks of the Rayleigh and Compton scattered peaks give a much higher background in the energy region between 8 and 12 keV in the case of the HPGe detector.

The relative (SRM 1577) and absolute (SRM 1832) limits of detection are shown in Fig. 8(a) and (b). Relative LDs of <0.1 ppm for elements of $Z > 25$ is achievable by using 14.4 keV for the efficient excitation of the lower Z elements. For $30 < Z < 38$, LDs at the 0.01 ppm level are reached in a measuring time of 1000 s. The absolute LD is <1 fg in 1000 s live time in the $Z > 22$ atomic number range [Fig. 8(b)]. For elements with overlapping peaks with the escape peak of the Compton peak, such as Cu, Zn and Se, the detection limit measured by the HPGe detector is significantly larger than that measured by the Si(Li) detector [Fig. 7(a) and 8(a)]. The intensities of the scattered peaks and hence those of their escape peaks are much larger in the case of thick samples. The effect of the escape peaks of the scattered peaks on the LD is negligible in the case of a thin sample [Figs. 7(b) and 8(b)]. The absolute LDs measured at 21 keV energy by the two detectors do not differ significantly for elements of $Z > 19$. The better LD measured by the HPGe detector for low-Z elements (such as Si and P) is caused mainly by its much lower background in this energy region. Also, the lower absorption of the MOXTEK window for low-Z elements is important: the transmission of Si Kα in an 8 μm Be layer is 0.84 whereas in the 3000 Å polymer and 400 Å Al layer it is about 0.94.

In order to investigate the effect of the measurement geometry on the spectra, the SRMs were measured at different measurement geometries (see Table 2 and Fig. 9). The solid angle of detection and the air path and volume of air seen by the detector (R, V) were determined by a collimator

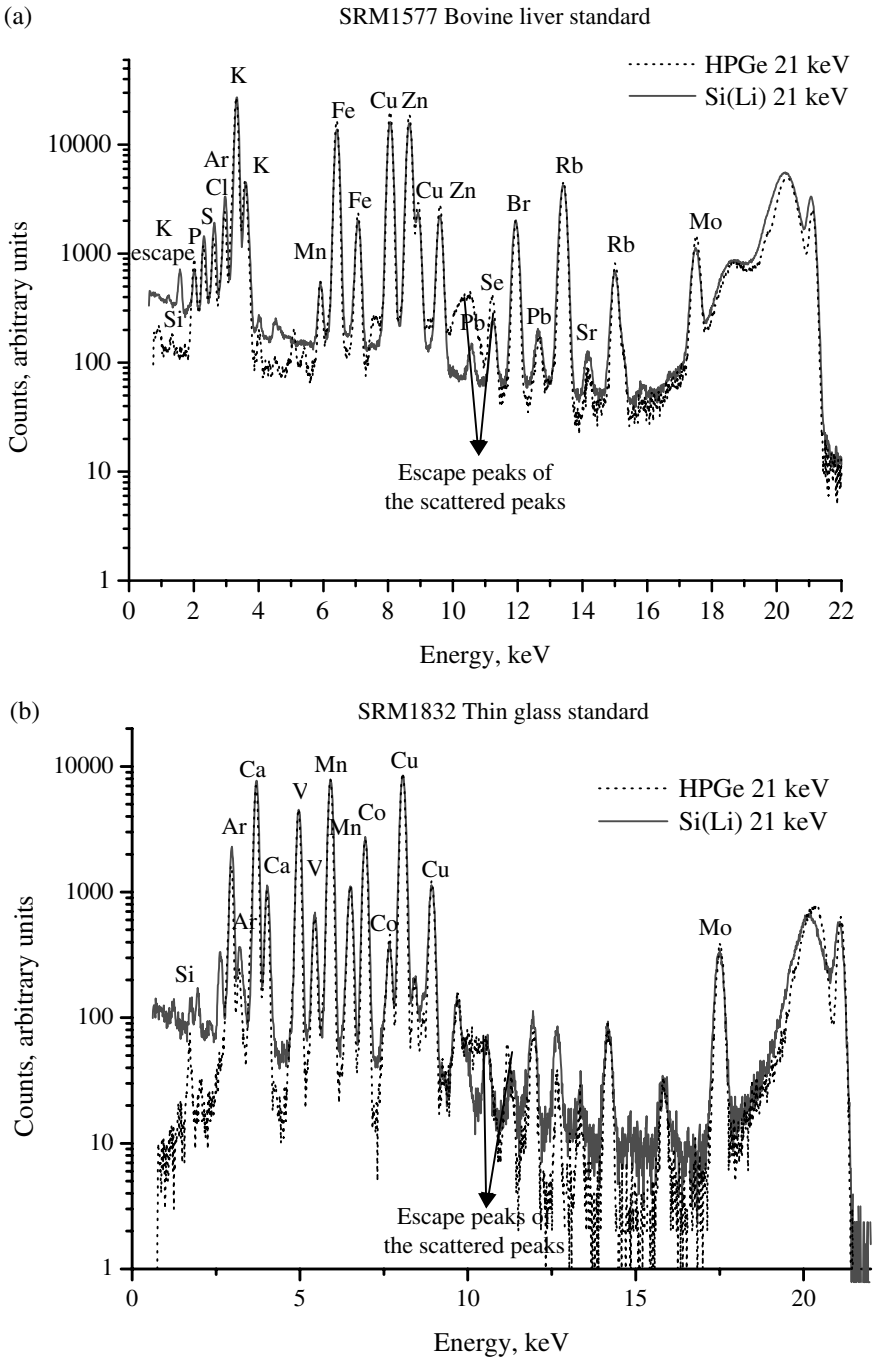

Figure 7. Measured spectra of (a) SRM 1577 bovine liver and (b) SRM 1832 thin glass standards by different detectors at 21 keV under similar measurement geometry. Measurement time 1000 s. The spectra were normalized to the same total counts. Measured spectra of (c) SRM 1577 bovine liver and (d) SRM 1832 thin glass standards by an HPGe (PGT) detector at 14.4 and 21 keV under identical measurement geometry. Measurement time 1000 s. The spectra were normalized to the same total counts.

consisting of two apertures of different hole diameters (R_1, R_2) and by the sample–detector distance. Similar solid angles of detection (Geom1 and Geom4, see Table 2) or similar air paths seen by the detector (Geom2 and Geom3) could be obtained by using appropriate combinations of apertures and sample–detector distance. The contribution of air scattering to the spectral background is proportional to the air path seen by the detector. The contribution of air to the intensity of the scattered peaks is more pronounced in the case of thin samples where the contribution from the sample itself becomes comparable to that of the air. In Fig. 10(a), the spectra of SRM 1832 thin standard measured for a 300 s live time at Geom4 and Geom1, respectively (similar solid angles but very different air paths), are shown. The two spectra were normalized to the same total number of counts. It is obvious that the intensities of the scattered peaks and that of Ar fluorescence are larger in the case of Geom4, clearly pointing to an increased contribution of air scattering. On the other hand, the reduced intensities of the characteristic x-ray lines of the low-Z elements, such as Si, Cl and Ca, show increased absorption in the longer air path; 75% of the Si, 35% of the Cl and 18% of the Ca intensities are absorbed in

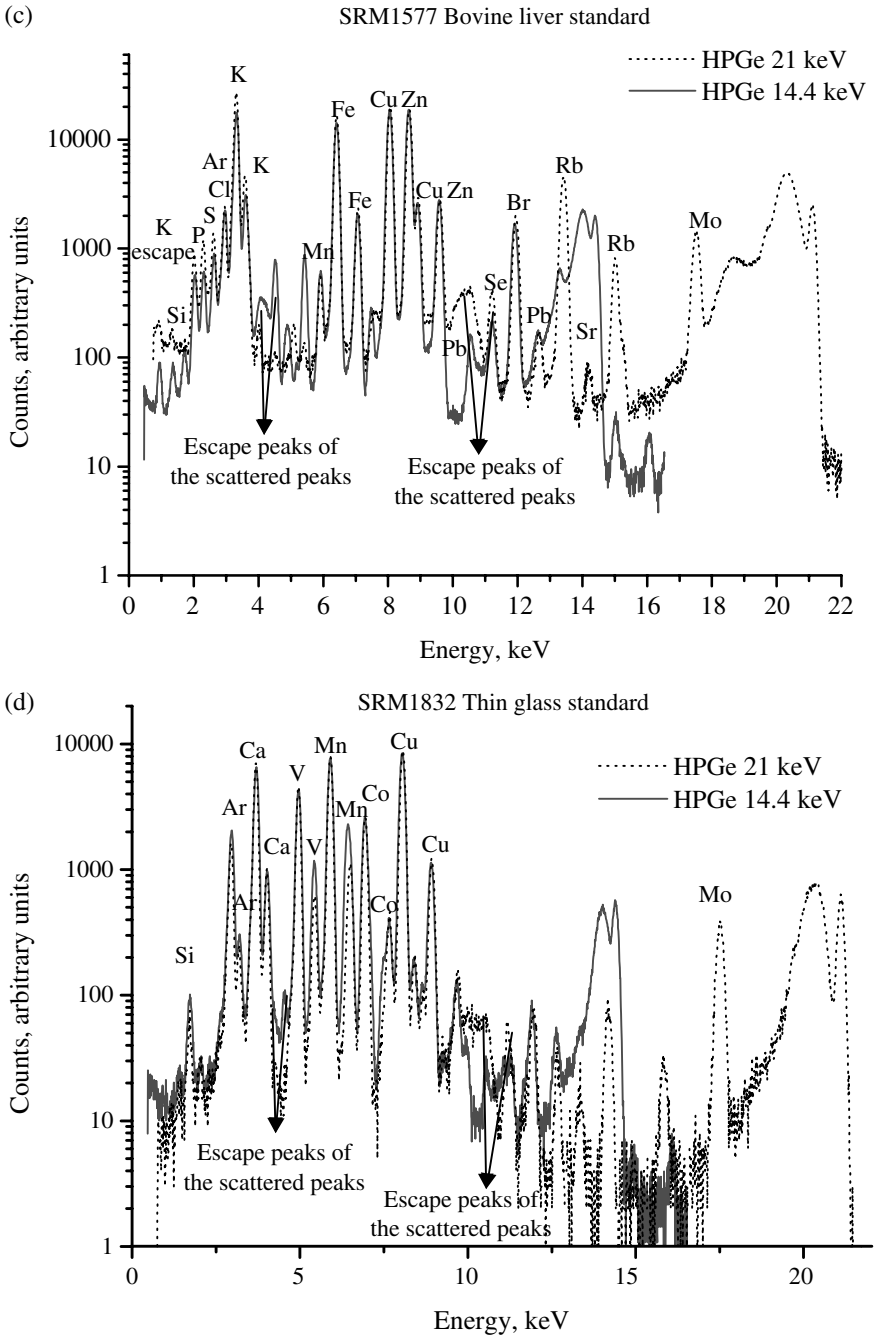

Figure 7. (*Continued*).

15 mm of air. The significant increase of the background in the lower energy part of the spectrum may also be the result of detector edge effects.

In order to make a distinction at low energies between air scattering and detector edge effects, a thin standard was measured with collimator B at different sample–detector distances [Geom3 and Geom4, see Fig. 10(b) and Table 2]. The approximately three times smaller solid angle of Geom4 was compensated by measuring for a three times longer live time in this case (300 s for Geom4 and 100 s for Geom3) in order to obtain similar total counts. The spectra were normalized to the same total counts. While the difference in the intensities of the scattered peaks and that of the Ar peak indicates the difference in the air path seen by the detector in the two different measurement geometries, there is no significant change in the low-energy background. This suggests that the increase in the lower energy background in Geom4 compared with Geom1 is mainly caused by increased incomplete charge collection due to edge effects of the detector.

In Fig. 11, the spectra of SRM 1577 are shown measured in Geom1 and Geom2. The difference in the solid angle was compensated by measuring for a live time of 1000 s in Geom2 and for 200 s in Geom1. The spectra are very similar except for the lower peaks of the low-*Z* elements because of the larger absorption due to the longer air path between the sample and the detector in the case of Geom2. The shoulder on the low-energy side of the Compton peak is caused by multiple scattering in the sample. The longer air path seen

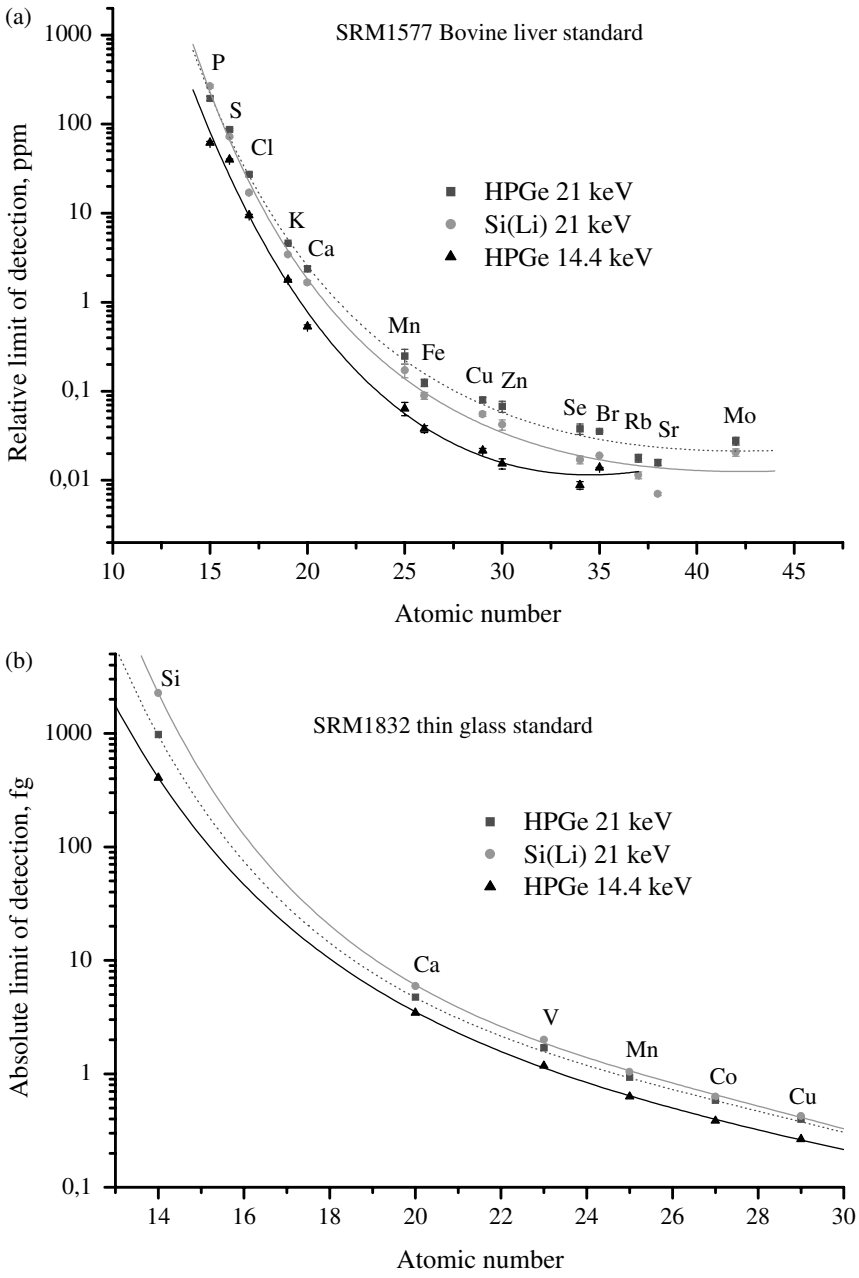

Figure 8. Relative and absolute limits of detection derived from the measured spectra shown in Fig. 7(a)–(d).

by the detector did not cause significant changes in the low-energy background.

CONCLUSION

A new user end-station ID18F is being built in the third experimental hutch of ID18 (ESRF, Grenoble, France). The use of the FZP and CRL in-line focusing devices having focal distances in the 0.5–2 m range has the advantage of easy alignment of the microprobe set-up, free space around the sample and the possibility of simultaneous fluorescence and diffraction (SAX and WAX) measurements. The size of the beam at the sample position can be changed easily by moving the sample out from the image plane. Depending on the focusing element used, beam sizes in the 1–5 μm (vertical) and 12–15 μm (horizontal) range can be achieved routinely.

The analytical characteristics of the new end-station were tested. Using a non-optimized temporary set-up, it was shown that the available relative detection limits are <0.1 ppm for elements of $Z > 25$. LDs down to a few ppb are a realistic goal for some elements on the basis of 1000 s live time measurements. Absolute LDs determined from the measurement of a thin glass standard are <1 fg for elements of $Z > 25$. Further improvement of the detection limit is predicted by using the optimized experimental set-up, two undulators in the 21.5–27 keV energy range and a side-by-side bent multilayer mirror.

Two different types of semiconductor detectors [Si(Li) and HPGe], were compared in the 6–30 keV energy region achievable at ID18F. The LDs with HPGe for elements with overlapping x-ray peaks with the escape peak of the Compton peak were significantly worse than those measured

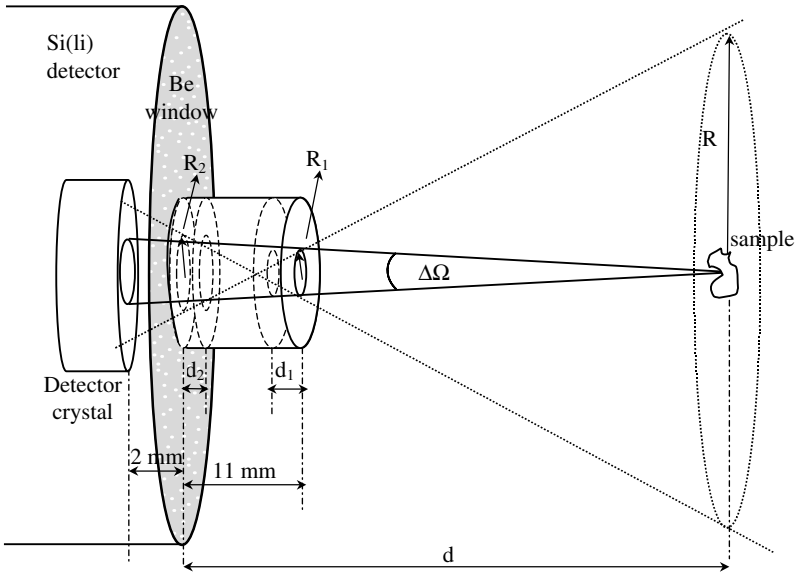

Figure 9. Schematic layout of the measurement geometry (top view, not to scale).

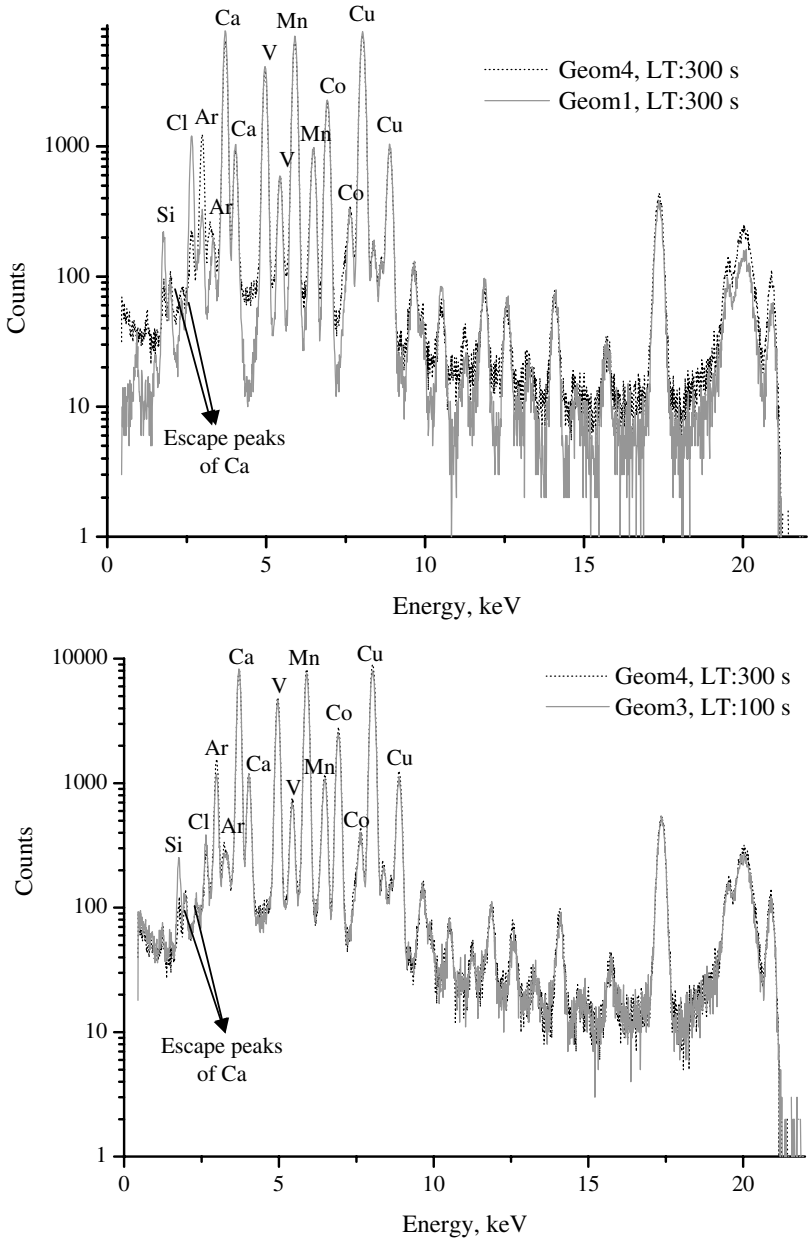

Figure 10. Measured spectra of SRM 1832 in (a) Geom1 and Geom4 and (b) Geom3 and Geom4 (see Table 2).

Table 2. Solid angles of detection and radii and volumes of the air seen by the detector under different measurement conditions

	Collimator A ($R_1 = 1$ mm, $R_2 = 2$ mm $d_1 = d_2 = 1$ mm)		Collimator B ($R_1 = R_2 = 4$ mm $d_1 = 4.2$ mm, $d_2 = 1$ mm)	
Parameter	Geom1 $d = 21$ mm	Geom2 $d = 36$ mm	Geom3 $d = 21$ mm	Geom4 $d = 36$ mm
$\Delta\Omega$ (sr)	6.49×10^{-3}	1.16×10^{-3}	2.26×10^{-2}	8.27×10^{-3}
R (mm)	1.86	3.9	5.0	9.6
V (mm^3)	48	457	413	3075
$e^{-\mu(\text{air},21\ \text{keV})\times 2\times R}$	0.999647	0.999259	0.999050	0.998178

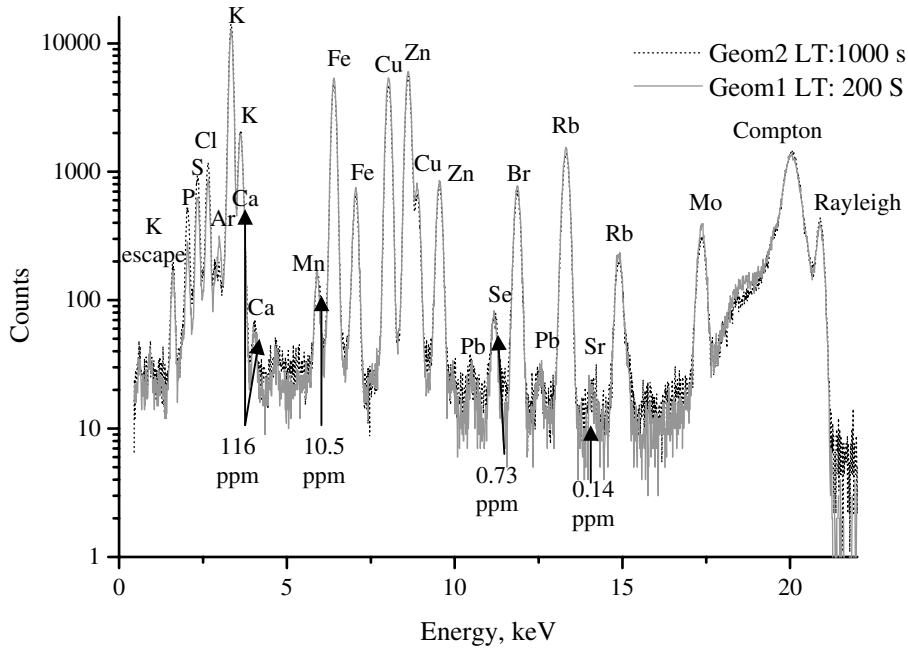

Figure 11. Measured spectra of SRM 1577 in Geom1 and Geom2 (see Table 2).

with the Si(Li) detector. On the other hand, the LD of HPGe is better in the low-energy region owing to the lower continuous background.

The effect of the measurement geometry on the peak-to-background ratio was investigated by measuring standard samples under different experimental conditions. The most significant portion of the spectral background appears to be caused by the edge effect of the semiconductor detector resulting in a significant decrease in the peak-to background ratio. Using a collimator with a large hole diameter results in an increase in air scattering and multiple scattering from a thick sample. Under the given measurement conditions the increase in the intensities of the scattered peaks did not have a very large effect on the low-energy background. In the case of a given solid angle, the best detection limits can be achieved by measuring at a small sample–detector distance with a collimator of small hole diameter.

Acknowledgements

We are grateful to IESS, Rome, Italy and to RWTH, Aachen, Germany for providing the FZP and CRL lenses for our work. We thank to the staff of ID18 for their help during our measurements at their beamline. Special thanks are due to John Morse and Cristophe Frieh for their continuous help during the detector test experiments.

REFERENCES

1. Rüffer R, Chumakov AI. *Hyperfine Interact.* 1996; **97/98**: 589.
2. Lai B, Yun WB, Legnini D, Xiao Y, Chrzas J, Viccaro PJ, White V, Bajikar S, Denton D, Cerrina F, Di Fabrizio E, Gentili M, Grella L, Baciocchi M. *Appl. Phys. Lett.* 1992; **61**: 1877.
3. Yun W, Lai B, Cai Z, Maser J, Legnini D, Gluskin E, Chen Z, Krasnoperova AA, Vladimirsky Y, Cerrina F, Di Fabrizio E, Gentili M. *Rev. Sci. Instrum.* 1999, **70**: 2238.
4. Snigirev A, Kohn V, Snigireva I, Lengeler B. *Nature* 1996; **384**: 49.
5. Lengeler B, Schroer C, Tummler J, Benner B, Richwin M, Snigirev A, Snigireva I, Drakopoulos M. *J. Synchrotron Radiat.* 1999; **6**: 1153.
6. Vincze L. PhD Thesis, Antwerp, 1995.
7. Van Espen P, Janssens K, Nobels J. *Chemom. Intell. Lab. Syst.* 1986; **1**: 109.
8. Nullens H, Van Espen P, Adams F. *X-Ray Spectrom.* 1979; **8**: 104.